

Height Dependency of Solar Eclipse Effects: The Ionospheric Perspective

Tobias G. W. Verhulst¹  and Stanimir M. Stankov¹ ¹Royal Meteorological Institute (RMI)—Solar-Terrestrial Centre of Excellence (STCE), Brussels, Belgium**Key Points:**

- The three-dimensional geometry of solar eclipses has to be taken into account for ionospheric studies
- The path of central eclipse at ionospheric altitudes can be significantly different from that at sea level
- There are large differences in geometry between eclipses

Supporting Information:

- Supporting Information S1
- Text S1
- Text S2

Correspondence to:T. G. W. Verhulst,
tobias.verhulst@oma.be**Citation:**Verhulst, T. G. W., & Stankov, S. M. (2020). Height dependency of solar eclipse effects: The ionospheric perspective. *Journal of Geophysical Research: Space Physics*, 125, e2020JA028088. <https://doi.org/10.1029/2020JA028088>

Received 7 APR 2020

Accepted 20 MAY 2020

Accepted article online 11 JUN 2020

Abstract A reliable interpretation of solar eclipse effects on the geospace environment, and on the ionosphere in particular, necessitates a careful consideration of the so-called eclipse geometry. A solar eclipse is a relatively rare astronomical phenomenon, which geometry is rather complex, specific for each event, and fast changing in time. The standard, most popular way to look at the eclipse geometry is via the two-dimensional representation (map) of the solar obscuration on the Earth's surface, in which the path of eclipse totality is drawn together with isolines of the gradually-decreasing eclipse magnitude farther away from this path. Such “surface maps” are widely used to readily explain some of the solar eclipse effects including, for example, the well-known decrease in total ionization (due to the substantial decrease in solar irradiation), usually presented by the popular and easy to understand ionospheric characteristic of total electron content (TEC). However, many other effects, especially those taking place at higher altitudes, cannot be explained in this fashion. Instead, a more detailed description of the umbra (and penumbra), would be required. This paper addresses the issue of eclipse geometry effects on various ionospheric observations carried out during the total solar eclipse of 21 August 2017. In particular, GPS-based TEC measurements were analyzed and eclipse effects on the ionosphere are interpreted with respect to the actual eclipse geometry at ionospheric heights. Whenever possible, a comparison was made with results from other eclipse events.

1. Introduction

Solar eclipses have a strong impact on the ionosphere because the majority of the ionization in the ionosphere is due to the direct solar radiation. During the eclipse itself a sharp decrease in the ionization level is observed, followed by a return to normal daytime conditions shortly after the end of the eclipse (Bamford, 2001; Stankov et al., 2017; Verhulst et al., 2016). Often the decrease in maximal ion density is also associated with a change in height of the ionospheric F_2 layer as well as changes in the temperature of both the neutral and ionized species (Rishbeth, 1968, 1970). Given the rapid onset and passage of eclipses, in comparison with the typical relaxation times of ionospheric disturbances, during a total solar eclipse the ionosphere is promptly forced out of both photochemical and diffusive equilibrium (Müller-Wodarg et al., 1998), and eclipse-associated perturbations can linger on after the local occurrence of the maximal eclipse. Consequently, some eclipse effects on the ionosphere come with a delay, which can be quite substantial in some circumstances (Hoque et al., 2016; Stankov et al., 2017). In addition to the direct impact locally, that is, along the path of obscuration, a solar eclipse can induce far reaching wave-like phenomena traveling away from the path (Abidin Abdul Rashid et al., 2006; Afraimovich et al., 2000; Altadill et al., 2001; Mošna et al., 2018; Verhulst & Stankov, 2018). Considering the complex response of the ionosphere, it is of particular importance that an accurate calculation of key characteristics of solar eclipses—such as timing, locations, and levels of obscuration—is carried out, and preferably provided in advance. Clearly, the availability of such information prior to a particular eclipse event would help the planning and execution of a dedicated monitoring campaign and facilitate the post-processing and analyses of results.

Calculation of the occurrence and circumstances of solar eclipses is complicated, compared to, for instance, lunar eclipses, because it depends on the precise location of the observer. The standard reference for the characteristics of past and future solar eclipses is the *Five Millennium Canon of Solar Eclipses* (Espenak & Meeus, 2009), provided by NASA and available through this url (eclipse.gsfc.nasa.gov). However, when this catalog of eclipses is used in the context of ionospheric research, some caution is required.

First, the apparent positions of the Sun and Moon depend on the altitude above sea level, and the changes in horizontal parallaxes between an observer on the ground and one at ionospheric altitudes is not negligible (Verhulst & Stankov, 2017). It has been shown in Stankov et al. (2017), in the context of the 2015 solar eclipse over Europe, that these geometric effects are indeed important in understanding the reaction of the ionosphere to the eclipse.

Second, since a significant part of the extreme ultraviolet (EUV) radiation is coming from the solar corona around the visible solar disk, the diameter of the corona has to be used as diameter of the Sun (Davies et al., 2001; Mrak et al., 2018). Contrary to the visible light, for which the solar disk can be assumed to be mostly uniform, the emitted EUV radiation varies strongly over the solar disk and corona (Hairston et al., 2018; Mrak et al., 2018). Since the EUV radiation is associated with active regions on the Sun, it cannot be precisely predicted long time in advance.

This paper is organized as follows. First, in section 2, we provide the calculations for the prediction and characterization of the geometry of solar eclipses in general, and show how the altitude above sea level can be taken into consideration. The resulting formulas, applied to the calculation of the path of central eclipse and the height dependent obscuration in either the visible or EUV spectrum, are implemented in Python as described in section 3. The main results are presented in the next two sections. In section 4 we show the results in relation to TEC measurements during the August 2017 eclipse. In section 5 the results for other recent and future eclipses, up to 2025, are provided. We further discuss in section 6 the ionospheric observations during the solar eclipses in 2015 and 2017, especially in light of the eclipse geometry calculations here presented.

2. Geometrical Calculations

Since the Sun cannot be considered a uniform radiator in the ionizing part of the spectrum, and the entire corona is never fully eclipsed, the precise limits of umbra and penumbra and the exact times of contacts are not very important for ionospheric applications. However, it is important to investigate the large-scale differences between the eclipses' paths and the timing of the eclipses' evolutions. For this purpose, we will consider the spatial and temporal variations in the curve of central eclipse with altitude. By definition, the curve of a central eclipse comprises those points where the axis of the shadow cone intersects a sphere with its midpoint at the center of the Earth.

The formulas given here are mostly based on the detailed derivations found in Chauvenet (1863). Our calculations are done in two steps: First, the path of central eclipse is calculated from the ephemerides in an specially constructed Cartesian coordinate system. Next the solution is transformed from these coordinates to latitude, longitude, vertical height above mean sea level, and universal time. In order to find the position of the shadow cone produced by the Moon, and the location of the observer relative to it, a coordinate system is defined in which the xy plane goes through the center of the Earth perpendicular to the axis of the shadow cone. Since this axis connects the center of the Sun and Moon, the z axis is taken through the center of the Earth, parallel to the line passing through the centers of the Moon and Sun and positive toward the Sun. See the left-hand panel of Figure 1, where M and S indicate the positions of the Moon and Sun and the origin O of the coordinate system is taken at the center of the Earth.

The coordinates of the point Z, where a line through the center of the Earth parallel to the Moon-Sun line meets the celestial sphere, are fully determined by the positions of the Sun and Moon. Let α_{M} , δ_{M} , and r_{M} ; α_{S} and δ_{S} ; and r_{S} be the right ascension, declination, and radial distance of, respectively, the Moon and the Sun. The coordinates of the Sun in a parallel coordinate system with its origin at the center of the Moon are given by

$$R \cos d \cos a = r_{\text{S}} \cos \delta_{\text{S}} \cos \alpha_{\text{S}} - r_{\text{M}} \cos \delta_{\text{M}} \cos \alpha_{\text{M}} \quad (1)$$

$$R \cos d \sin a = r_{\text{S}} \cos \delta_{\text{S}} \sin \alpha_{\text{S}} - r_{\text{M}} \cos \delta_{\text{M}} \sin \alpha_{\text{M}} \quad (2)$$

$$R \sin d = r_{\text{S}} \sin \delta_{\text{S}} - r_{\text{M}} \sin \delta_{\text{M}} \quad (3)$$

with a , d , and R the right ascension, declination and radial distance in this system of coordinates. The direction of the z axis is now given by a and d .

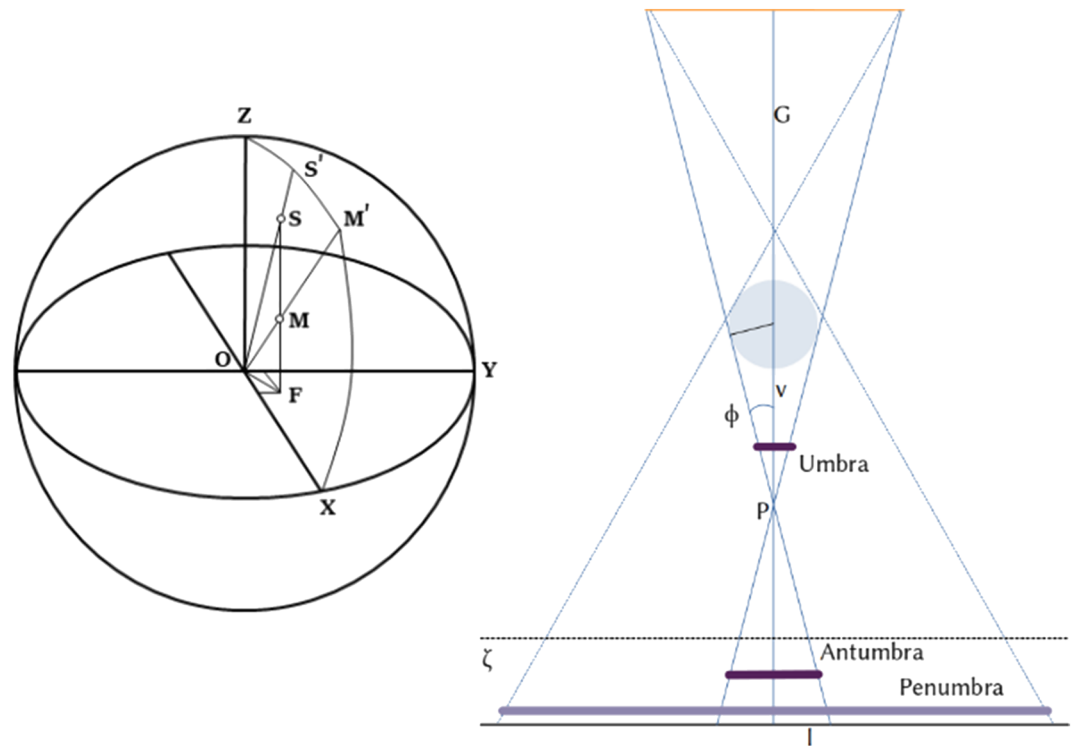


Figure 1. Schematics of the solar eclipse geometry, after Chauvenet (1863). (left) Orientation of the Cartesian coordinate system oriented with the z axis along the line connecting the Sun and the Moon. M and S are the positions of the Moon and Sun, and m' and s' their projection on the celestial sphere. O is the center of the Earth and F the origin of the translated coordinate system. (right) Schematic view of the geometry of the umbra and penumbra cones during a solar eclipse. v is the distance from the point P to the center of the Moon, while G is the distance between the centers of the Moon and Sun. l is the radius of the umbra on the fundamental plane, that is, the plane through the center of the Earth and perpendicular to the line connecting the centers of the Sun and Moon. ζ is the distance of the observer above the fundamental plane.

The x and y coordinates of the axis of the shadow cone in these coordinates are then given by

$$x = r_{\odot} \cos \delta_{\odot} \sin (\alpha_{\odot} - a) \quad (4)$$

$$y = r_{\odot} (\sin \delta_{\odot} \cos d - \cos \delta_{\odot} \sin d \cos (\alpha_{\odot} - a)) \quad (5)$$

Clearly, the x and y coordinates for the Sun and the Moon are by construction identical in this system of coordinates, and they can alternatively be calculated from the solar instead of lunar ephemerides.

The coordinates ξ , η , and ζ of an observer can be calculated in the same fashion:

$$\xi = (R_{\oplus} + h) \cos \varphi \sin (\mu - a) \quad (6)$$

$$\eta = (R_{\oplus} + h) (\sin \varphi \cos d - \cos \varphi \sin d \cos (\mu - a)) \quad (7)$$

$$\zeta = (R_{\oplus} + h) (\sin \varphi \sin d + \cos \varphi \cos d \cos (\mu - a)) \quad (8)$$

Here, ϕ is the colatitude and μ the sidereal time of the observation, R_{\oplus} is the radius of the Earth and h is the altitude above the ground. It is possible to take into account the variations in the Earth's radius with the latitude of the observer, but since these variations are smaller than the variations in for instance hmF_2 —the height of the main ionospheric electron density peak—we will use a constant radius. The distance $R_{\oplus} + h$ can be interpreted as the distance from the center of the Earth, and from this the height above local mean sea level can be obtained to the desired precision by using a realistic model for the shape of the Earth.

Consider now the angle ϕ between the edge of the umbral cone and the line connecting the Sun and the Moon, as depicted in the right-side panel of Figure 1. From this figure it is clear that

$$\sin \phi = \frac{R_{\odot}}{G + v} = \frac{R_{\text{M}}}{v}, \quad (9)$$

where the distance G between the centers of the Sun and Moon is given by

$$G = \sqrt{r_{\text{M}}^2 - 2r_{\text{M}} r_{\odot} (\cos \delta_{\odot} \cos \delta_{\text{M}} \cos (\alpha_{\odot} - \alpha_{\text{M}}) + \sin \delta_{\odot} \sin \delta_{\text{M}}) + r_{\odot}^2}. \quad (10)$$

From Equation 9 one finds easily the distance v between point P and the center of the Moon:

$$v = \frac{GR_{\text{M}}}{R_{\odot} - R_{\text{M}}}, \quad (11)$$

and therefore,

$$\sin \phi = \frac{R_{\odot} - R_{\text{M}}}{G}. \quad (12)$$

Note that the point P can either fall between the fundamental plane and the Moon, as in the figure, or below the fundamental plane. The former case corresponds to annular eclipses, the latter situation indicates a total eclipse. In the rare cases where P falls between the fundamental plane and the observer, the latter will see a total eclipse, while a hypothetical observer at the center of the Earth would see an annular eclipse.

A similar calculation for the penumbra—shown as dashed lines in the right panel of Figure 1—gives

$$\sin \phi = \frac{R_{\odot} + R_{\text{M}}}{G}. \quad (13)$$

In the following derivations we will only consider the umbra, as we are primarily interested in the path of central eclipse. A complete derivation of the penumbral case can be found in the literature, for instance Chauvenet (1863).

The distance between point P in Figure 1 (right) and the principal plane is equal to $z_{\text{M}} - v$, where z_{M} is the z coordinate of the Moon. Thus:

$$\tan \phi = \frac{l}{z_{\text{M}} - v}, \quad (14)$$

and taking into account Equation 11:

$$l = \left(z_{\text{M}} - \frac{GR_{\text{M}}}{R_{\odot} - R_{\text{M}}} \right) \tan \phi. \quad (15)$$

For an arbitrary observer at a distance ζ above the fundamental plane, the radius L of the shadow is then

$$L = l - \zeta \tan \phi. \quad (16)$$

The distance of this observer, with coordinates ξ and η in the plane parallel to the fundamental plane, from the axis of the shadow is given by $\sqrt{(x-\xi)^2 + (y-\eta)^2}$. Thus, the edge of the shadow is described by

$$\sqrt{(x-\xi)^2 + (y-\eta)^2} = l - \zeta \tan \phi. \quad (17)$$

From this equation, the entire shape of the umbra shadow on the Earth can be obtained (and in the same manner for the penumbra, as indicated above). In order to obtain the path of the central eclipse, it can be observed that this consists of the points for which $\xi = x$ and $\eta = y$ and therefore $\zeta \tan \phi = l$. Thus, we have

obtained the rectangular coordinates ξ , η , and ζ of the central eclipse from the solar and lunar ephemerides. It now remains to transform from this system of coordinates to longitude, latitude, and radial distance by inverting the Equations 6–8. Multiplying Equation 8 with $\cos d$, Equation 7 with $\sin d$, and subtracting gives

$$\zeta \cos d - \eta \sin d = (R_\delta + h) \cos \phi \cos(\mu - a). \quad (18)$$

$\mu - a$ can now be obtained from Equations 6 and 18:

$$\mu - a = \arctan \frac{\xi}{\zeta \cos d - \eta \sin d} = \omega - t_{ST} - a. \quad (19)$$

Here ω is the longitude and t_{ST} the time. Squaring Equations 6 and 18 and adding them gives

$$\xi^2 + (\zeta \cos d - \eta \sin d)^2 = (R_\delta + h)^2 \cos^2 \phi, \quad (20)$$

and thus

$$\phi = \frac{\sqrt{\xi^2 + (\zeta \cos d - \eta \sin d)^2}}{R_\delta + h}. \quad (21)$$

Using the fact that the square of the radial distance $(R_\delta + h)^2 = \xi^2 + \eta^2 + \zeta^2$, it is also possible to obtain h as a function of the coordinates ξ , η , and ζ , for instance, to find the altitude at which the eclipse is maximal. However, in the current work we are looking for the longitude and latitude of the central eclipse for a given h .

One final problem to be solved is to determine the sign of ϕ , which is ambiguous in 21. This ambiguity can be solved by isolating $\sin \phi$ from 8:

$$\sin \phi = \frac{\zeta}{(R_\delta + h) \sin d} - \cos \phi \cot d \cos(\mu - a), \quad (22)$$

and thus (since $\cos \phi$ does not depend on the sign of ϕ):

$$\text{sgn } \phi = \text{sgn} \left(\frac{\zeta}{(R_\delta + h) \sin d} - \cos \phi \cot d \cos(\mu - a) \right). \quad (23)$$

Thus, we have found ϕ and ω —the latitude and longitude of the curve of central eclipse—in function of ξ , η , and ζ , which in turn are calculated from the solar and lunar ephemerides.

As an example, we will now calculate the position of the central eclipse for the 21 August 2017 eclipse at the moment of greatest eclipse at sea level, 18:26 UT (rounded to the nearest minute, calculations can be done with higher temporal precision if desired). This example will be calculated using the visible light solar disc, without taking into account the extended corona. The solar and lunar ephemerides at this time are given in Table 1. These ephemerides were obtained from the `pyephem` Python package, as described in section 3. The rectangular coordinates for both objects are obtained by a simple coordinate transformation (Vallado, 1997).

Using Equation 10 the distance between the Sun and Moon is found to be $G = 1.50952 \cdot 10^8$ km. From Equation 11 it then follows that $v = 378,871$ km. Since v is larger than r_\oplus , the point P in Figure 1 is below the fundamental plane, indicating a total eclipse. So far, the calculations are independent of the observer. The rest of the calculation, however, do depend on the observers altitude h . In Table 2, the coordinates ξ , η , ζ , as well as the longitude and latitude of the maximal eclipse are listed for observers at 0 km, 350 km, and 1000 km above sea-level.

The longitude and latitude obtained at sea level agree with the values available in the literature (Esenak, 2014); compare also with the maps shown in Figure 2. As we will discuss further below, the paths at different altitudes tend to be closest together around the time of maximal eclipse. Nevertheless, this example shows that differences of several degrees in both longitude and latitude can be observed even in that case.

Table 1
Ephemerides of the Sun and Moon on 21 August 2017 at 18:26 UT

	☉	☾
r [km]	1.51324e+8	372,103
α [hr]	10:04:04	10:04:32
δ [°]	11:51:43	12:16:28
x [km]	-1.2955e+8	-318,415
y [km]	0.7176e+8	175,541
z [km]	0.3111e+8	79,107

3. Implementation

The method of calculating the path of central eclipse described in the previous section requires knowledge of the lunar and solar ephemerides. Calculating accurate and precise ephemerides is a complicated task, see, for instance, Nautical Almanac Office (1961) and Meeus (1985, 1998) for some details. Several well-established software libraries for this are however available for various programming languages. We have implemented the calculations in Python, and the code used is available as supporting information to this paper. The freely available Python package `pyephem` was used for this purpose. This package uses the XEphem routines, which

implement the semianalytic VSOP87 (Bretagnon & Francou, 1988) planetary theory to calculate the ephemerides of the Sun and Moon. While `pyephem` is now obsolete and one could use the latest version of the `astropy` library instead, this is not required for our purposes.

In order to validate the results of our calculations, we compared the paths we obtained for various eclipses at sea level with those given in the established Canon of Solar Eclipses made available by NASA (Espenak, 1987). In all cases we found very good agreement between the result of our sea-level calculations and the paths given in the canon. One example can be seen in comparing the left-side panel of Figure 2 with the sea-level curve shown in the top panel of Figure 10.

The first of the provided scripts, `eclipsePathCalculator.py`, defines the method `centralEclipse(t, height = 0)`, which returns the latitude and longitude of the central eclipse at time t and altitude `height`. The other methods provided are subroutines called by the method to calculate the central eclipse. At the beginning of the code a constant `sunMultiplier` is defined. This multiplier is applied to the solar radius, which features in some of the calculations, as can be seen in the formulas in section 2. Note that even though we are only calculating the path of central eclipse, the solar radius does still play a role. Setting this constant to variables higher than 1 can be used to take into account the extended corona as a source of ionizing radiation. Examples of the paths calculated by this script can be seen below in Figures 6 to 9.

The second script, called `obscurationCalculator.py`, can be used to calculate the percentage of the solar disk obscured by the Moon, as seen by a specific observer at a given time. Using again the ephemerides of the Sun and Moon provided by the `pyephem` package, calculating the obscuration is a straightforward application of the circle-circle intersection formulas (Weisstein, 2020). The main method defined in this script is `obscurationProfile(begin, end, lat, lon, [z = 0])`, which returns a list of obscurations in percentage for the period between `begin` and `end`, with a time resolution of 1 min (see the script itself for more details). The same `sunMultiplier` constant is used in this script as well in order to calculate the obscuration using an extended disk, as an approximation for taking into account the radiation of the corona. Examples of the output of this script, including the effect of the `sunMultiplier` parameter, are shown in Figure 12 below.

4. The American Eclipse of 2017

Figure 2 shows the map of the solar eclipse path at sea level. The eclipse started over the Pacific Ocean, with the first external contact of the penumbra at 15:46:52 UT. The path of totality then crossed the entirety of North America, entering from the North West (U.S. Oregon) to the South East (U.S. South Carolina) before ending over the Atlantic Ocean with the final contact of the penumbra at 21:04:24 UT. The greatest eclipse occurred at 18:25:32 UT at a location with coordinates of 36.67°N, 272.33°E, where the path width was 114.7 km.

Figure 3 shows the differences in the three key eclipse characteristics—the zenith angle, obscuration, and time of the maximal eclipse—at two different altitudes, at sea level (about 0 km) and at the mean ionospheric level (about 300 km), plotted in the same manner it was done by Stankov et al. (2017). In the figure, the values at the ionospheric height (denoted

Table 2
Coordinates of Central Eclipse for Different Observer Altitudes on 21 August 2017 at 18:26 UT

	0 km	350 km	1,000 km
ξ [km]	734	734	734
η [km]	2,687	2,687	2,687
ζ [km]	5,738	6,125	6,832
Latitude [°]	36.67	35.30	33.14
Longitude [°]	272.50	271.92	271.08

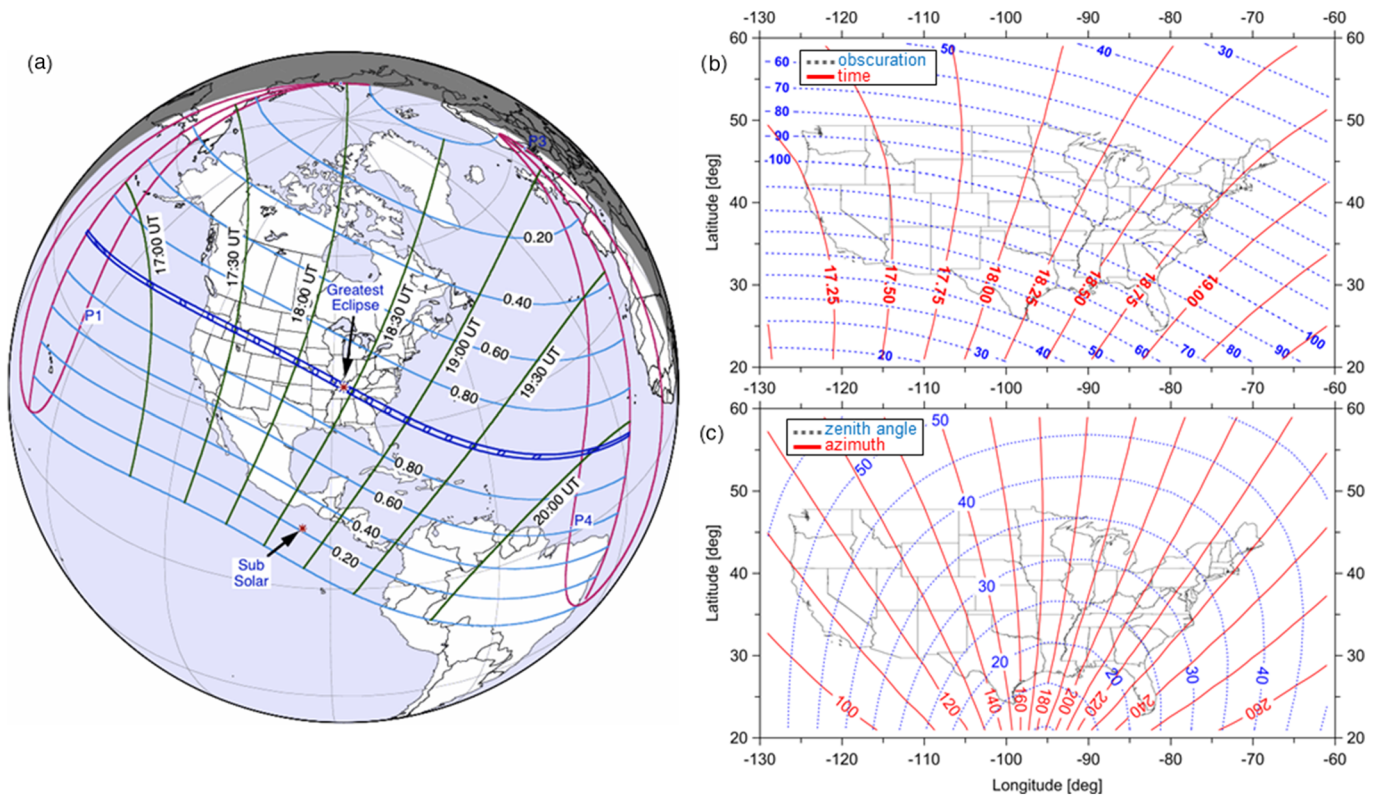


Figure 2. Eclipse geometry at sea level. (a) Schematic (credit: NASA) of the solar eclipse on 21 August 2017 at the Earth's surface. The path of the total solar eclipse is denoted by the strip bounded by dark blue curves, while paths of the partial (0.80, 0.60, 0.40, and 0.20 magnitude) eclipse are plotted with light blue curves. The progression of the greatest eclipse is marked by green curves with time stamps (UT). (b) Times of the maximum eclipse (solid red lines) and maximum obscuration levels (dotted blue lines) over North America. (c) Azimuth (solid red lines) and zenith angle (dotted blue lines) at the maximum eclipse over North America. Note: Cylindrical equidistant mapping is applied in (b) and (c).

with solid curves) are compared with the values at the sea level (denoted with dashed curves). The observed changes in geometry, going from sea level to ionospheric height, are highlighted by using red arrows. Clearly, all three parameters appear on the map differently at different altitudes. The isocurves (i.e., the curves of constant parameter values) at higher altitudes are at new places and their shapes are slightly different. With regard to the zenith angle (top panel), the isocurves appear as concentric semioval curves centered on the subsolar point. Obviously, the difference between the zenith angle at ground and ionospheric levels increases away from the subsolar point and can be as large as 5° (at $50\text{--}60^\circ\text{N}$). It has been shown already (e.g., Stankov et al., 2017) that a smaller zenith angle of the umbra causes a larger depletion in the total ionization.

Concerning the obscuration (middle panel), the altitudinal difference between the isocurves of the same obscuration level increases away from the subsolar point, in northeast direction. While the difference at lower latitudes is negligible, the change in the north ($50\text{--}60^\circ\text{N}$) is about 3 to 4° . The observed altitudinal changes are more or less uniform along the isolines. Also, these changes do not depend on the obscuration levels. However, higher obscuration levels at ionospheric altitudes cause larger depletions in the ionization levels. The time of the maximum eclipse (bottom panel) also changes with altitude. The differences in the times at sea level and at higher altitudes change in the course of the eclipse. In the initial phase of the eclipse, due to the Sun's elevation and azimuth, the maximum eclipse in the west appear on the ground before the maximum in the ionosphere. As the eclipse event progresses, the difference becomes smaller and smaller and at around the time of the maximum eclipse the difference disappears completely (i.e., the eclipse occurs at the same time at different altitudes along the corresponding isoline). Afterward, the maximum eclipse on the ground lags the maximum at ionospheric heights, and this lag is increasing progressively in the later phases of the eclipse.

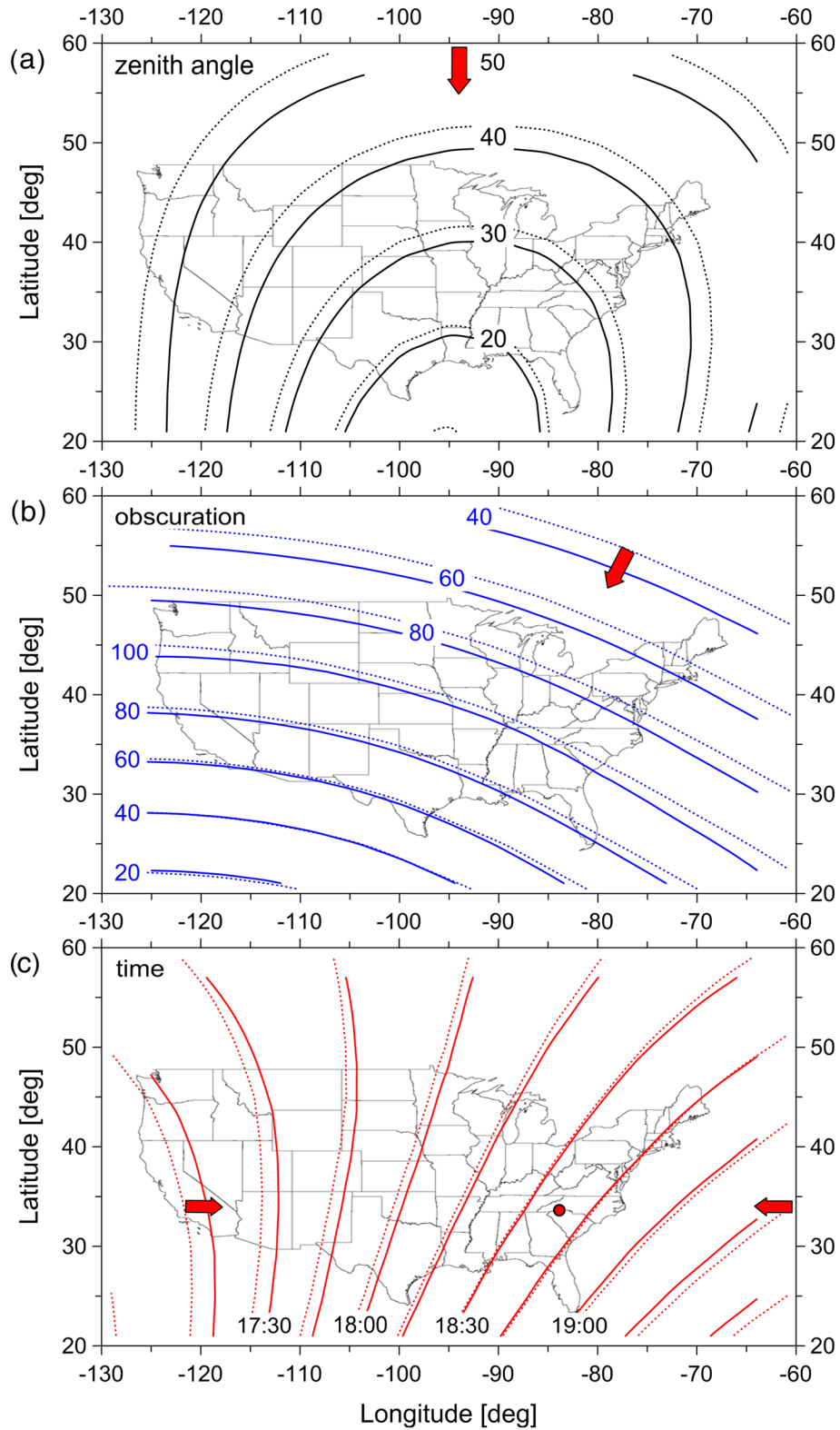


Figure 3. Differences in eclipse geometry (Earth's curvature ignored) at ground level (dashed curves) and ionospheric height of 300 km (solid curves): zenith angle (a), obscuration (b), and time (c) at the eclipse maximum. The changes in geometry, going from sea level to ionospheric height, are highlighted by (red) arrows.

Figure 4 presents the effects of the eclipse on the regional ionosphere via maps of the key ionospheric characteristic, the TEC. The left column contains maps from the reference day, 16 August 2017, while the corresponding maps from the eclipse day, 21 August 2017, are given in the middle column. To facilitate the analysis of the eclipse effects, maps have been produced of the TEC relative difference:

$$TEC_{rel} = \frac{TEC_{ecl} - TEC_{ref}}{TEC_{ref}}, \quad (24)$$

calculated at each grid point from the corresponding TEC values on the eclipse day (TEC_{ecl}) and the reference day (TEC_{ref}). The resulting difference maps, given as relative percentage deviation, are displayed in the right column.

The TEC maps from the reference day show the regular morning TEC increase appearing first in the south-east (SE) corner and progressing steadily toward the west (W). The corresponding TEC maps from the eclipse day shows a similar pattern. However, a pronounced decrease starts developing in the northwest corner (along the total eclipse path) around 17:00 UT, which expands later in SE direction. The effect is clearly seen on the difference maps. The first map (16:00 UT), based on data collected shortly after the nominal start of the eclipse at sea level, shows that above the territory of the United States the eclipse day TEC is lower than the reference day TEC by 5–10%. The opposite is observed in the SE (i.e., the sunward direction) where the relative difference increases by up to 10–20%. On the following map, at 17:00 UT, the abovementioned area of negative difference (depression) is shown significantly expanded in the SE direction at the expense of the positive difference area. In the following hour the depression area widened further and several patches of negative values exceeding 25%, appear in the NW as well as in the NE and SE, that is, on both sides of the totality path. At that time (18:00 UT) the Moon shadow has already reached the 100°W meridian and was heading toward the area of the maximum eclipse on the east coast of the continent. The next map at 19:00 UT shows two distinct patches formed, one on each side of the totality path, where the minimum values reach 40–45% below the reference values. In the next couple of hours, these two patches eventually merge into one larger patch in the SE which, at 21:00 UT, have minimum values of 45–50% below the reference values in this area. At the same time, the ionosphere has already recovered in the NW part of the continent. The depression persisted, although to a smaller extent and magnitude, for another hour or so. In fact, the last map (at 23:00 UT) indicates that the ionosphere in the SE might not have recovered completely even by the early hours of the next day.

The TEC difference maps showed that different locations experienced different levels of electron density depletion and that the depletion occurred at different times. First, to establish what the maximum depletion of TEC was and where it occurred, all TEC_{rel} maps within the time interval from 17:00 UT to 23:00 UT were processed and the minimum TEC_{rel} value picked up for each grid point. The resulting map, Figure 5a, shows that the maximum depletion was more than 15–20% almost everywhere in the covered area. A strip of stronger depletion, 25–35%, stretches from NW to SE along the totality path. Toward the east coast, the strip widens substantially and the depletion become much stronger. The strongest depletion, of more than 50%, was recorded in the SE, east of the Caribbean Sea. Interestingly, the maximum depletion was reached on a patch where the maximum obscuration was about 70–90% rather than in the area of complete obscuration. Note that the map of the maximum depletion shows the absolute minimum at each grid point irrespective of the exact time at which it occurred. To find out when the maximum depletion occurred with respect to the maximum eclipse at each location, at each grid point we subtracted the time of the maximum eclipse from the time of the maximum TEC_{rel} depletion. The resulting map is shown in Figure 5b, where positive values indicate delays. In the band where the obscuration was above 50%, the delay was mostly in the range of 30–60 min, but in some areas it exceeded 120 min. Even larger delays (in excess of 300 min) were observed in the SW which is difficult to explain if the TEC maps were accurate. Also difficult to explain are the negative values in the northeast part of the map, meaning that the maximum depletion was observed ahead of the time of the maximum obscuration.

5. Solar Eclipses up to 2025

In Figures 6 and 7, the paths of central eclipse are shown calculated for all central eclipses between 2019 and 2025 at various altitudes. The path at the ground level is shown in black color, while the colored curves show

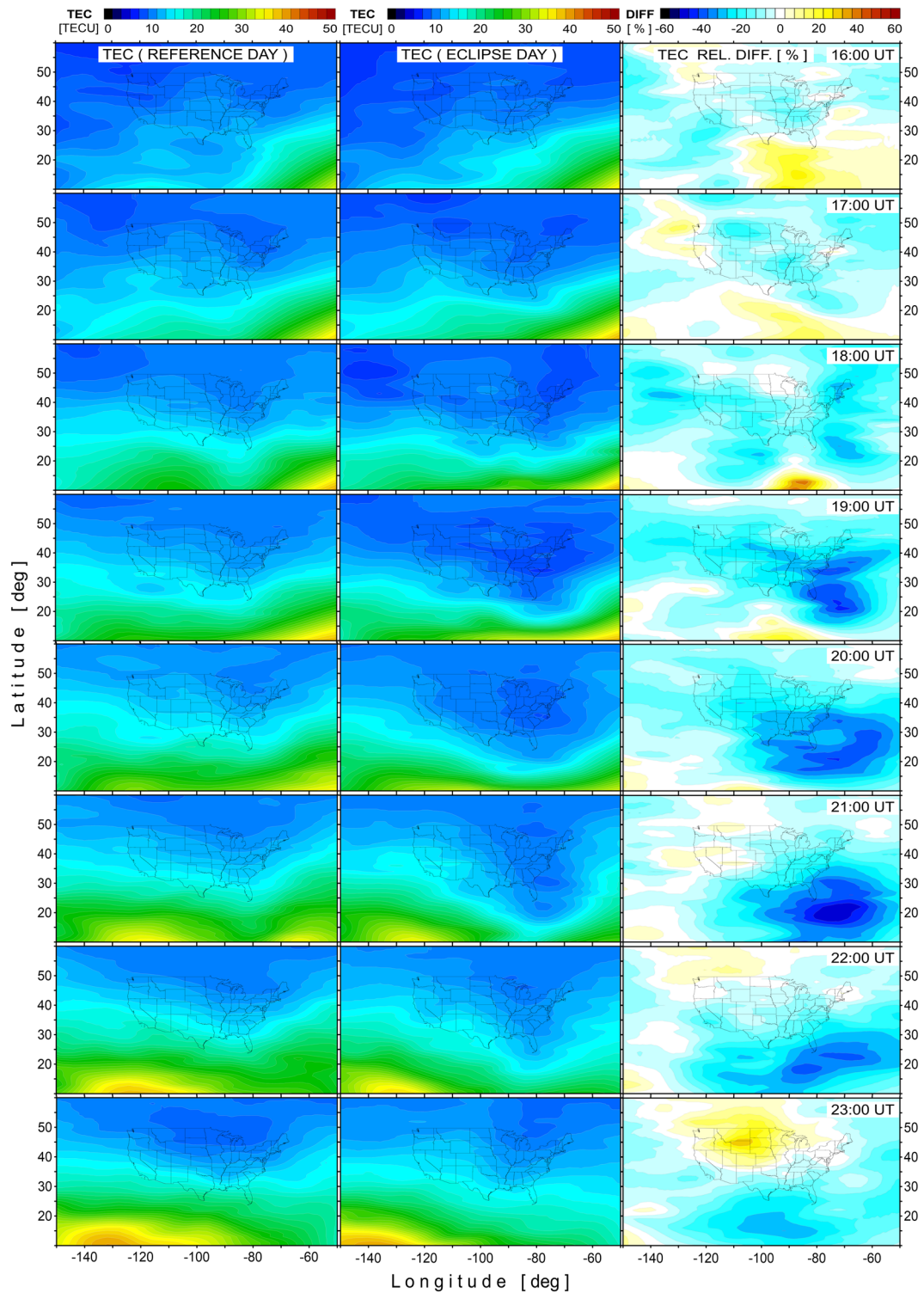


Figure 4. TEC response to the solar eclipse on 21 August 2017. The USTEC maps (credit: NOAA) during the reference day, 16 August 2017 (left column), and the eclipse day, 21 August 2017 (middle column), from 16:00 UT (top row) to 23:00 UT (bottom row), together with the relative deviation (in percentage) of the eclipse-day values from the corresponding reference day values (right column).

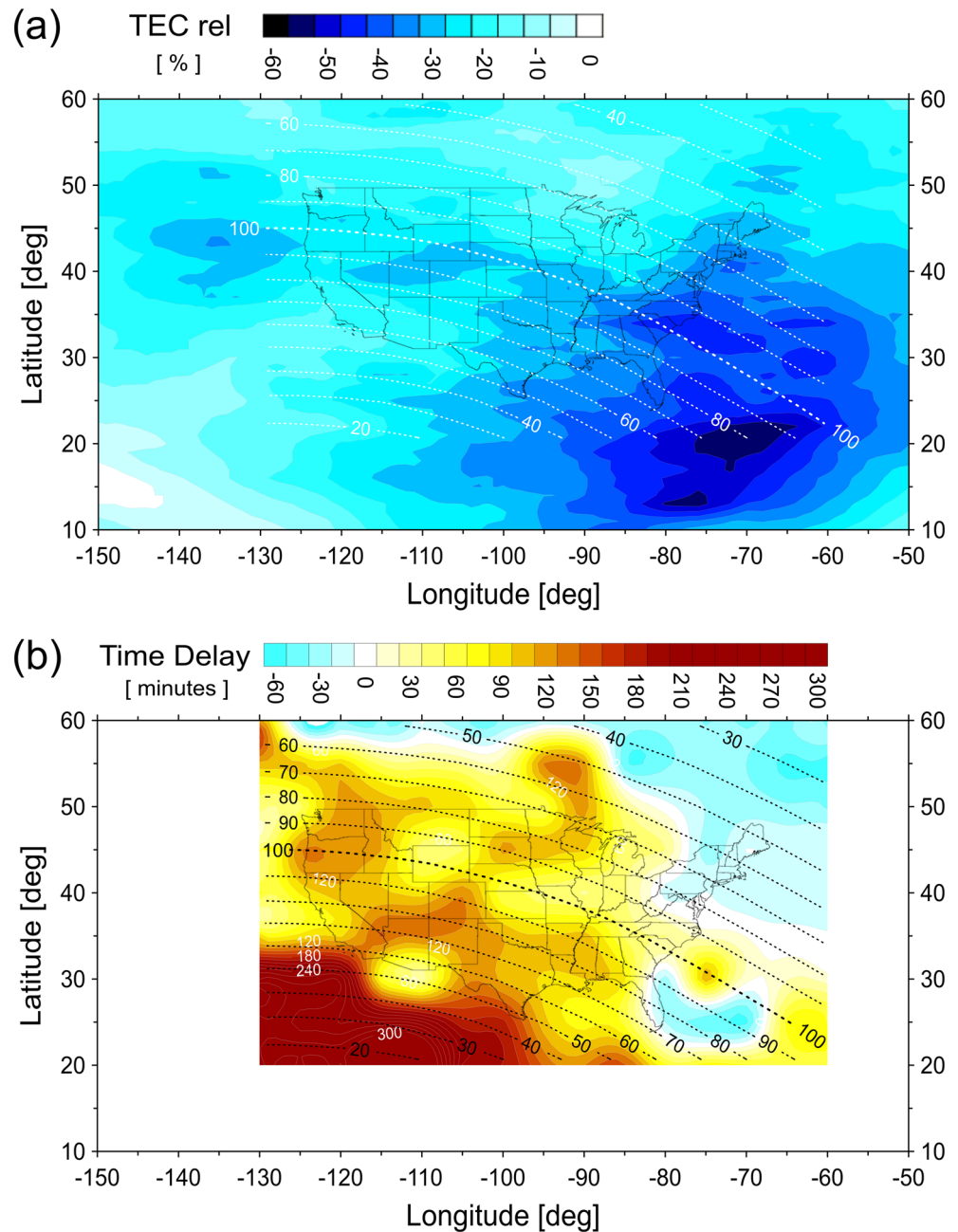


Figure 5. (a) Map of the maximum TEC depletion during the eclipse. (b) Map of the time delay of the maximum TEC depletion from the maximum obscuration. For reference, the obscuration levels at sea level are also plotted (dashed curves).

the paths at 100, 350, 500, and 1,000 km altitude. Note that while all maps in Figures 6 and 7 are produced using the same equirectangular projection, the scales are very different between them. In some cases, for instance, the eclipses in October 2022 over Russia or in March 2025 over Canada and Greenland, the eclipse does not reach totality at sea level but does so at higher altitudes. In these cases the altitudes where there is no central eclipse are not shown. The eclipse on 29 March 2025 is somewhat peculiar in this regard. Although this is a partial eclipse at sea level—and is identified as such, with a magnitude of 0.855, in the existing catalogs such as Espenak (2014)—even down to a typical ionospheric peak height of 350 km, a total eclipse takes place.

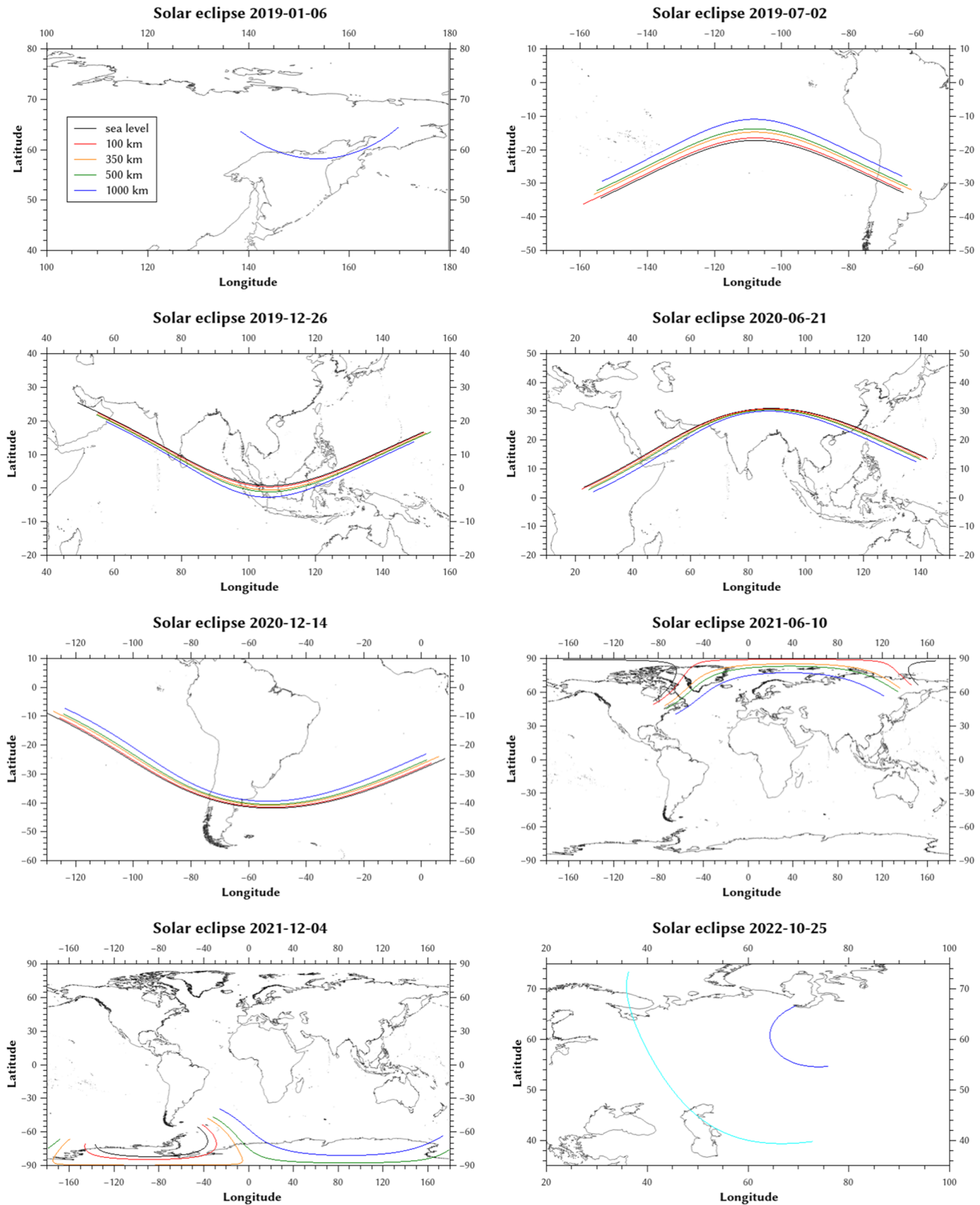


Figure 6. Central paths for solar eclipses from 2019 to 2022 at various altitudes. All maps are made using equirectangular projection. The black line shows the path at ground level, red at 100 km, orange at 350 km, green at 500 km, and blue at 1,000 km. If a curve is not shown, it means the eclipse at that altitude is a partial one. Note that because of the varying shape of the paths, the horizontal and vertical scales are not identical in all panels.

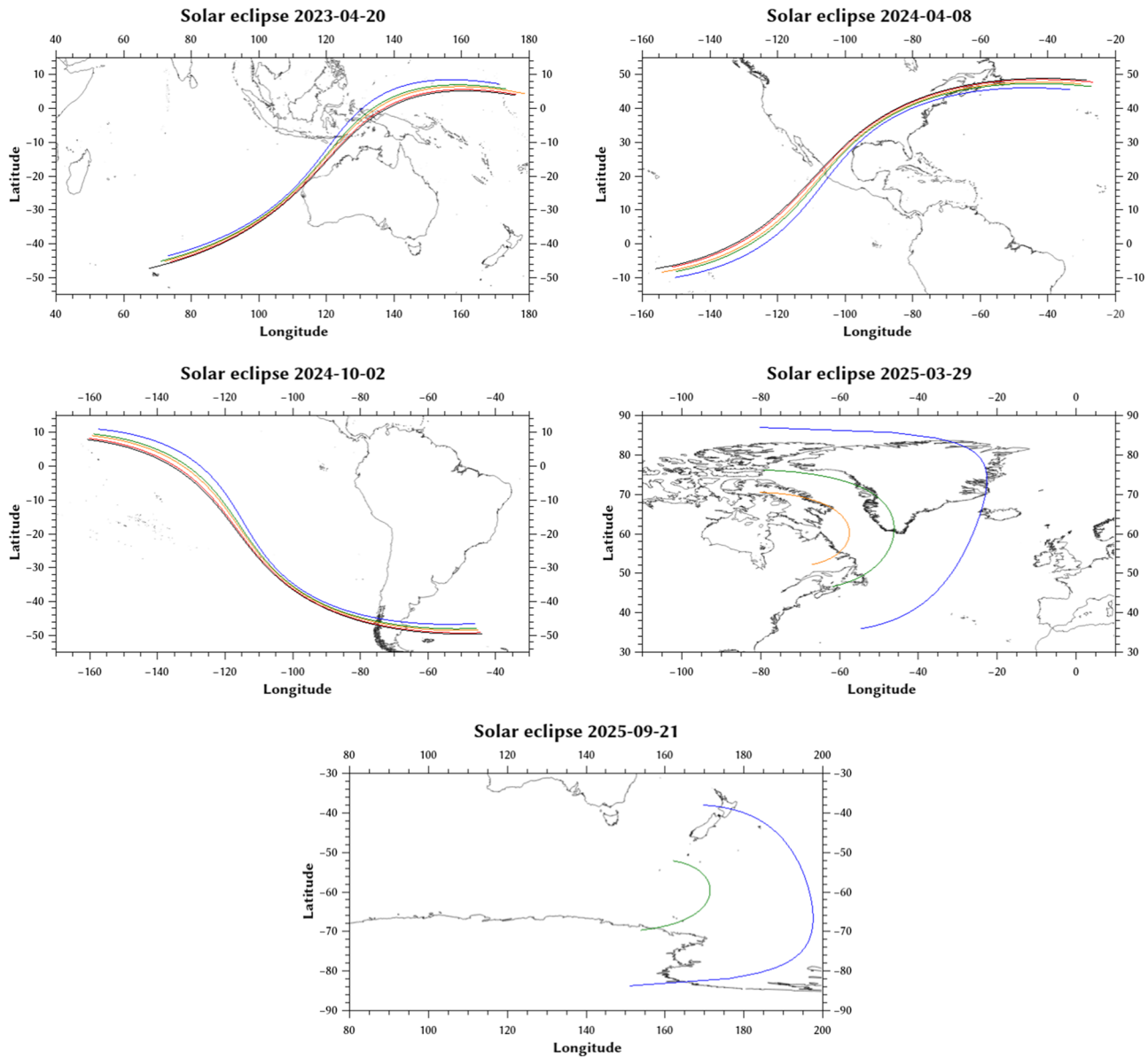


Figure 7. Continuation of Figure 6, showing the path of central eclipse for solar eclipses from 2023 to 2025. See the caption to Figure 6 for explanation.

Several systematic effects can be observed in the height dependency of the central eclipse paths. In Figure 1, a situation with the Sun in zenith is shown, resulting in a right angle between the center of the shadow cone and the surface. When the sun is at a lower elevation, the center of the shadow cone will arrive at a smaller angle. This will result in the path of the central eclipse at sea level being farthest away from the line between the centers of the Earth and the Sun, and paths at higher altitudes being progressively closer to this line—see also Stankov et al. (2017). Usually, this means that a path at higher altitude is closer to the equator than a path at a lower altitude. Exceptions arise when the path of an eclipse crosses the equator. Some examples of this are the eclipses on 26 December 2019 and 2 February 2024. In the case of the December 2019 eclipse, it can also be noted that the central path at sea level does not cross over into the Southern Hemisphere, but the one at 1,000 km altitude does. The position of the Earth-Sun line depends of course on the season.

It is also evident from the maps in Figures 6 and 7, and understandable when considering the geometry, that the separation between paths at various altitudes is generally larger in the polar regions than at lower latitudes. On the maps for the eclipses of 10 June and 4 December 2021, occurring, respectively, over the

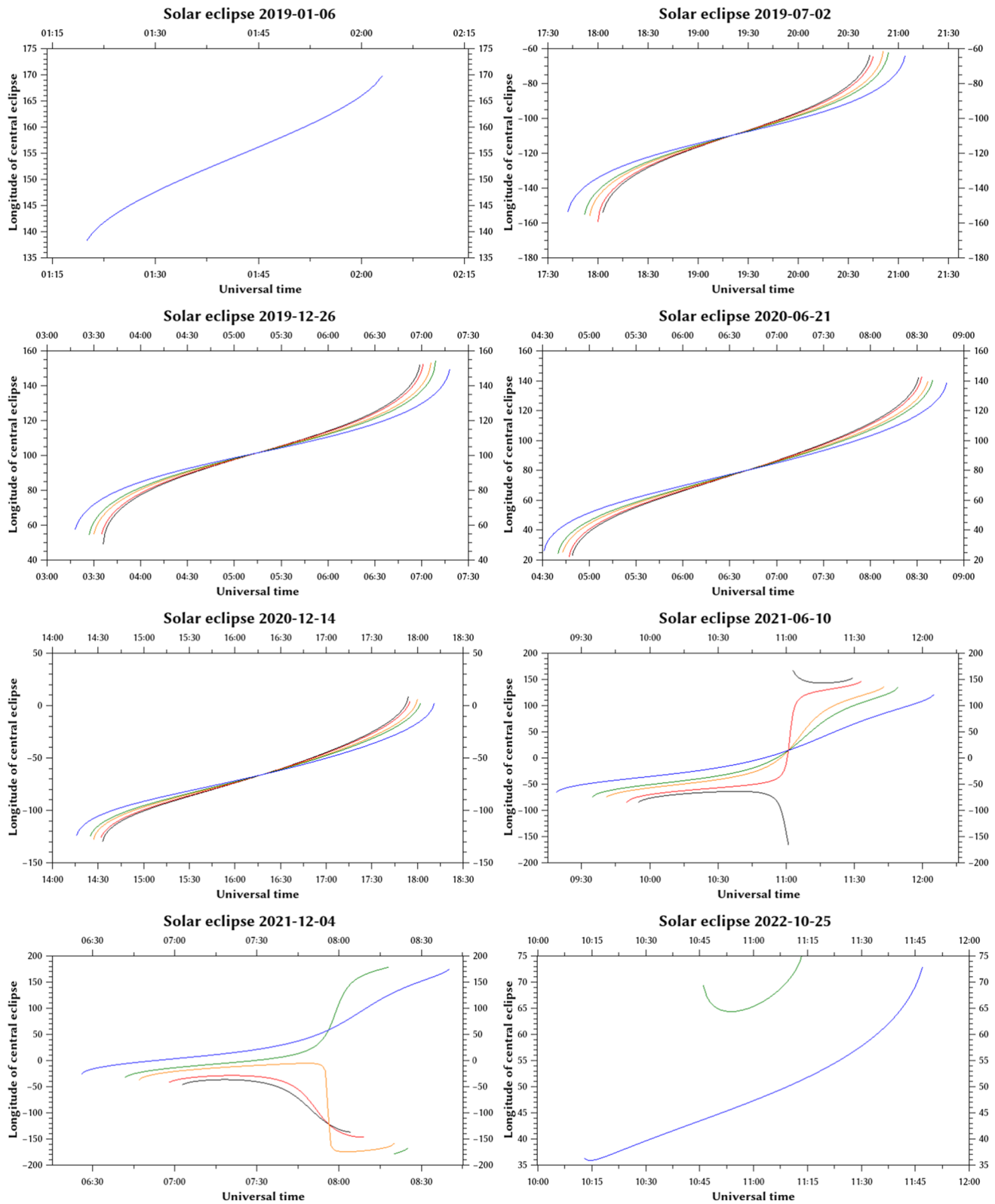


Figure 8. Plot of the longitude of the central eclipse as a function of time for the events between 2019 and 2022. The same colors are used as in Figures 6 and 7: The black line shows the path at ground level, red at 100 km, orange at 350 km, green at 500 km and blue at 1,000 km. The different shape of the curves for the events in 2021 are due to these eclipses occurring over the polar region. The longitudes of central eclipse at some fixed time changes sign with altitude; see also the corresponding maps in Figure 6.

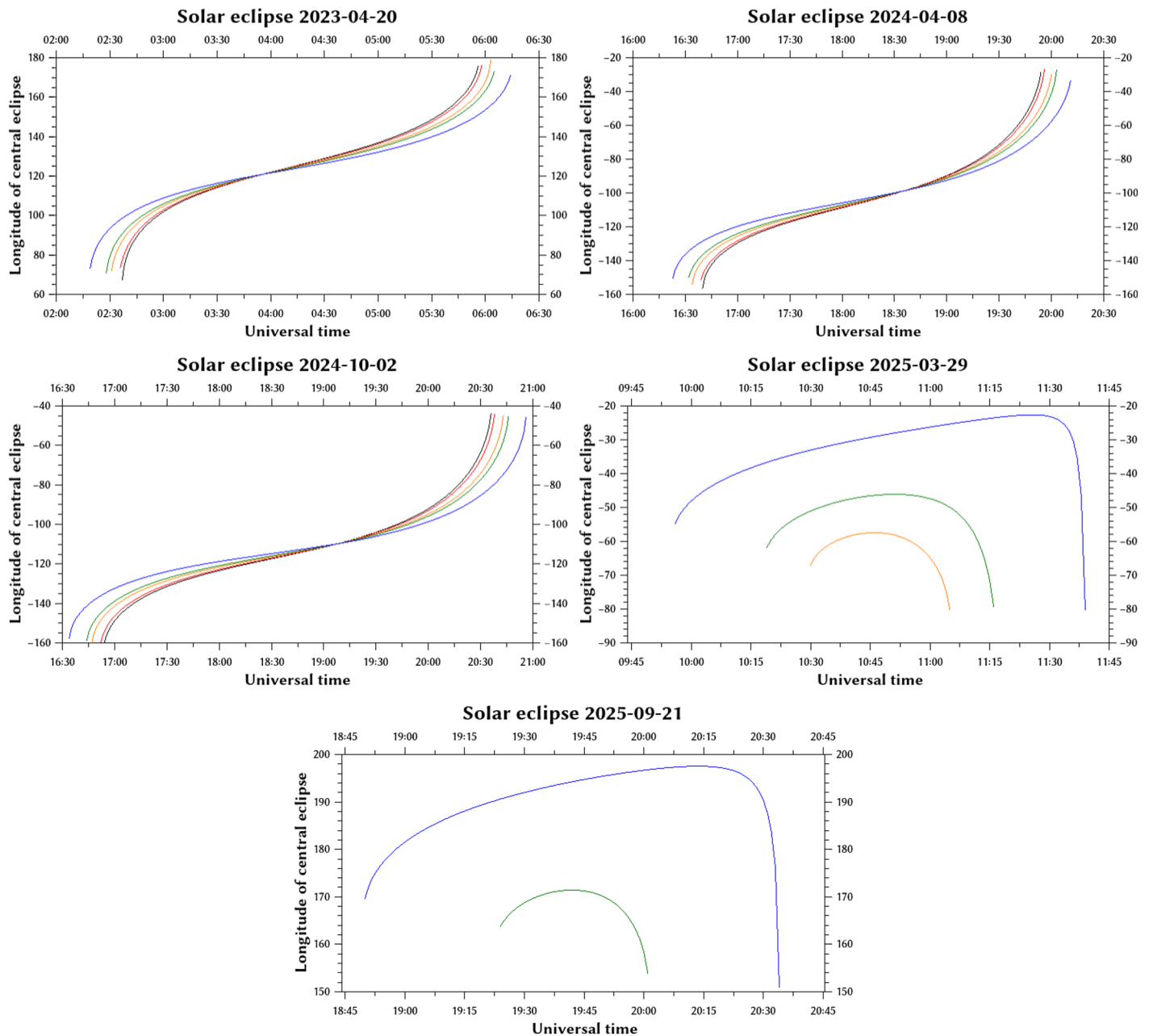


Figure 9. Continuation of Figure 8, showing the path of central eclipse for solar eclipses from 2023 to 2025. See the caption to Figure 8 for explanation.

Arctic and Antarctic regions, separations of up to 40° in latitude between the paths at sea level and at 1,000 km altitude can be observed. Note that the paths at high latitudes look somewhat distorted due to the equirectangular projection used in the maps. The appearance of the central eclipse paths at different altitudes in different longitude sectors that can be seen for both 2021 eclipses is due to tilt of the axis of the Earth compared to the ecliptic plane. In a polar projection the different paths would appear next to each other, similar to the pattern seen for eclipses at lower latitudes.

In Figures 8 and 9, the time evolution of the longitude of the central eclipse is shown for the same events, at the same range of altitudes. There are some peculiar cases, when the event happens over one of the poles or for the eclipses where the umbra does not reach the surface of the Earth. For all other cases, however, the time evolution looks very similar. The eclipse starts earlier and ends later at greater altitudes, as expected.

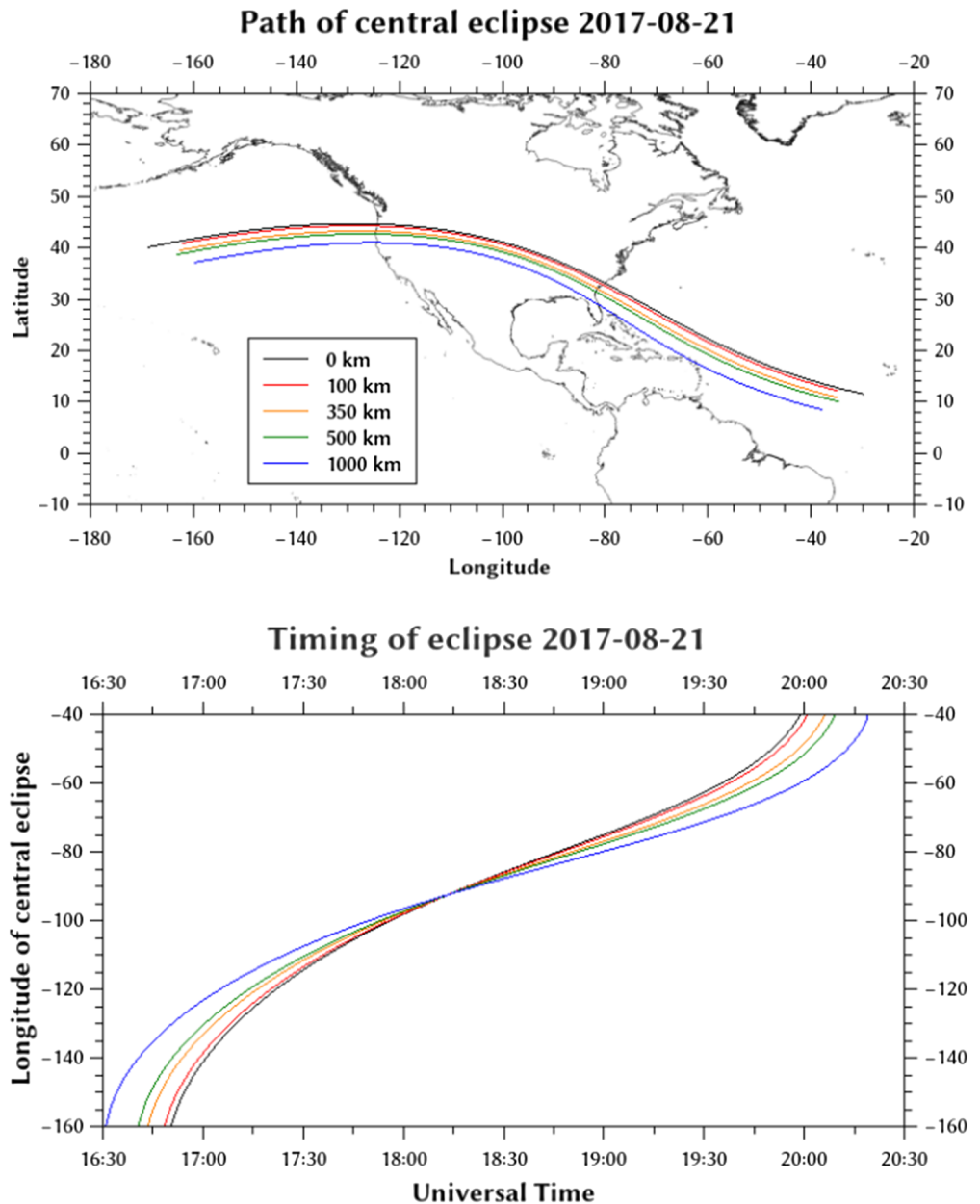


Figure 10. The path of central eclipse for 21 August 2017 at different altitudes. The black curves shows the path at sea level, the red one at 100 km, orange at 350 km, green at 500 km, and blue at 1,000 km altitude. The top panel shows the geographical location of the central eclipse (map using equirectangular projection), while the bottom panel shows the longitude of central eclipse as a function of time.

The difference in start and end time between 1,000 km height and sea level is always about 20 to 30 min. Although the paths of the central eclipse remain geographically separated at all times, as is evident from Figures 6 and 7, they do all coincide at one longitude at a certain time. This is the time and longitude where the maximal eclipse occurs with the Sun at its zenith.

6. Discussion

In section 4, observations were presented showing that the depletions in TEC seen over North-America during the 2017 total solar eclipse are shifted significantly, both in space and time, with respect to the central path of the eclipse calculated at sea level. In the top panel of Figure 10 the path of the central eclipse is

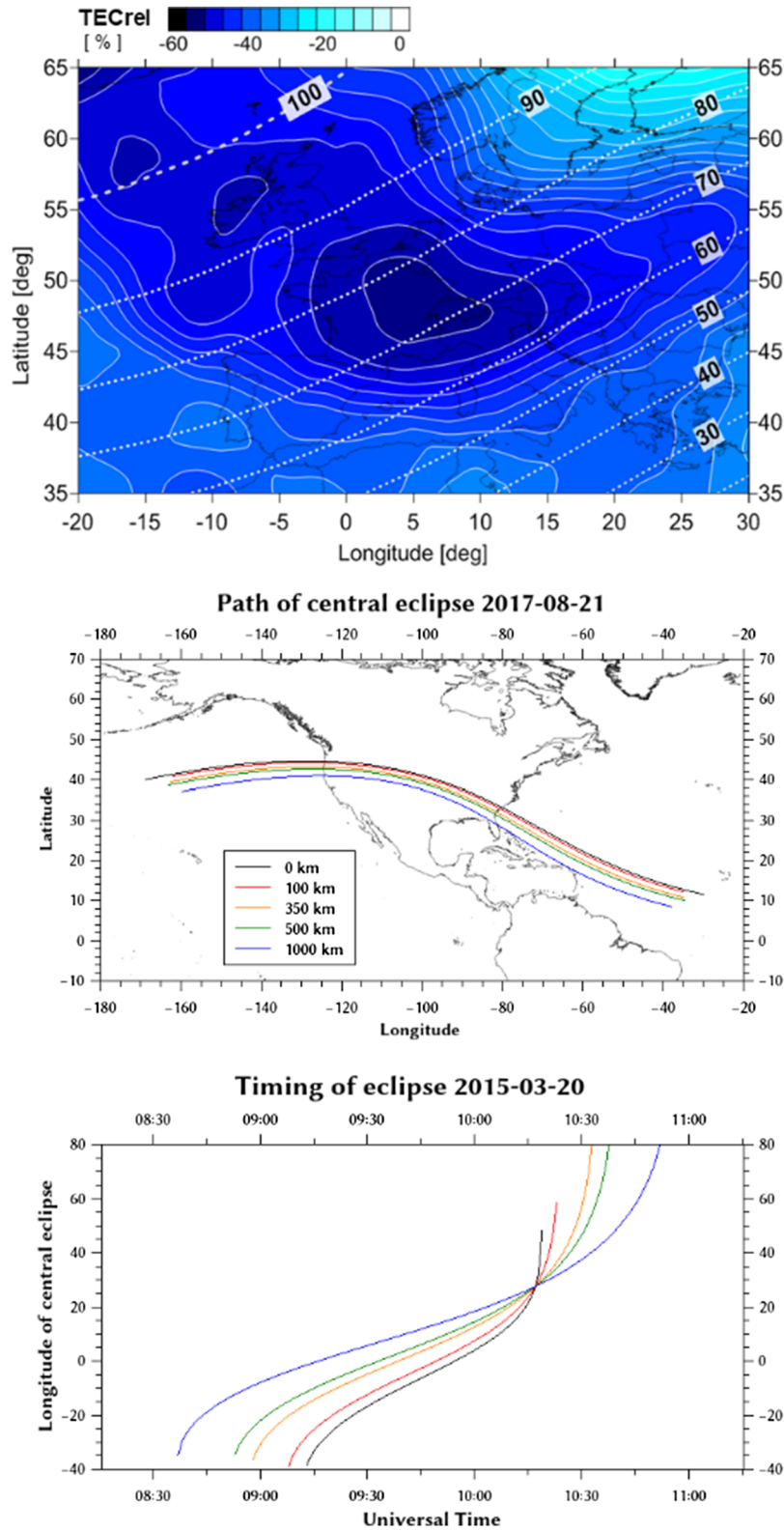


Figure 11. TEC depletion and paths of central eclipse for the 20 March 2015 solar eclipse over Europe. The top panel shows the maximal TEC depletion, similar to the top panel of Figure 5 for the August 2017 event (after Stankov et al., 2017). The middle panel shows the paths of central eclipse at various altitudes from sea level to 1,000 km. The bottom panel shows the longitude of central eclipse as a function of time, for the same altitudes.

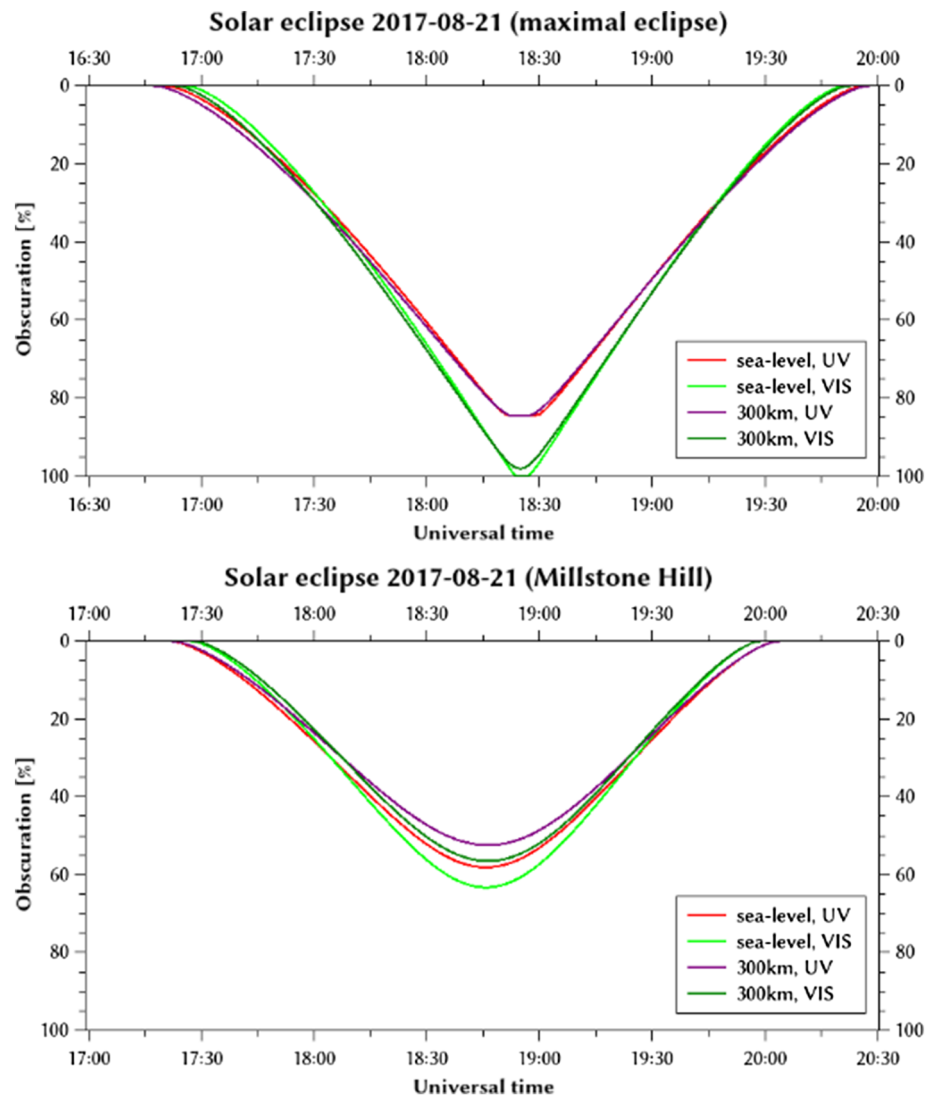


Figure 12. Visible light (dark and light green) and UV (purple and red) obscuration profiles, at sea level and 300 km altitude, for the point of maximal eclipse (top panel) and the Millstone Hill observatory (bottom panel). Note that the time scale is shifted by 30 min between the two panels.

shown at different altitudes. Comparing these paths to the TEC depletion shown in Figure 4 and the top panel of Figure 5, it can be seen that the main TEC depletion coincides with the path of central eclipse at altitudes of 500 to 1,000 km. This is to be expected, since this region of the ionosphere contains a significant fraction of the TEC. The effect of the different time evolution of the eclipse at various altitudes—shown in the bottom panel of Figure 10—is not clear. This is partially because the beginning and end of the eclipse, where the time differences are the clearest, happened over regions with relatively fewer measurements, or none at all. The maximal eclipse occurred over the continental USA, where a lot of TEC data are available but the time differences are minimal. In addition, various processes in the ionosphere itself can influence the timing of the maximal depletion, such as the effect of temperature changes and transport processes. Such effects have been discussed extensively in the literature before, see, for instance, Stankov et al. (2017), and references therein.

Even though the August 2017 eclipse occurred at relatively low latitudes, the separation between the central paths at sea level and in the topside ionosphere is between 5 and 10°. It can be seen in Figures 6 and 7 that this separation increases further for eclipses occurring at higher latitudes. Since the reaction of the

ionosphere to an eclipse is mostly dependent on the eclipse path at altitudes between 500 and 1,000 km, this shows the importance of taking into account the full three-dimensional geometry of the solar eclipse.

The top panel of Figure 11 presents the relative TEC depletion over Europe during the solar eclipse of 20 March 2015 (Stankov et al., 2017). The middle panel shows again the path of the central eclipse at heights ranging from sea level to 1,000 km altitude. Similar to what was observed during the 2017 eclipse, the maximum TEC depletion does not appear on the path of totality at sea level but in a region experiencing only 70–80% obscuration. When analyzing the central path at 1,000 km altitude, however, it can be seen that the path crosses precisely the region with the largest TEC depletion. For this eclipse, the final part of the event was observable by the high density of GNSS receivers in Europe, and the time-delay shown in the bottom panel of Figure 11 does match the observations described in Stankov et al. (2017). These observations are therefore consistent with those from the 2017 eclipse in illustrating that the eclipse path in the topside ionosphere should be considered rather than the one at sea level.

Although the time differences are shown to be smallest around the maximal eclipse, some effects can still be seen by looking at the evolution of obscuration at this location. The top panel of Figure 12 shows the evolution of the obscuration at the location of maximal eclipse for the August 2017 event. The green curves show the obscuration of the visible light solar disk at ground level and at 300 km altitude, around the height of the ionospheric F_2 peak. It can be seen that, while at ground level there is a period (calculated to last for 160.1 s) of 100% obscuration, the eclipse at ionospheric altitude above this location is not total. The highest obscuration reached is 98.9% at 18:25 UT. The purple curves represent the obscuration in the ultraviolet (UV), assuming a homogeneous UV radiation source. As discussed already in section 1, there is no total eclipse in the UV, and the highest obscuration at both altitudes is the same. However, it can be seen that the period of maximal obscuration is slightly longer at sea-level. It is also evident in both the visible light and UV curves that the onset and maximum eclipse happen slightly earlier at 300 km altitude. On the other hand, the eclipse ends earlier at sea-level. Therefore, the total duration of the event is shorter on the ground than it is in the ionosphere.

It is evident from Figures 8 and 9 that the differences in timing between the eclipse at sea level and at ionospheric altitudes is limited to about 30 min earlier or later. Some additional advance or delay can be explained by considering the EUV emitting corona instead of the visible solar disk only. However, even this combined effect is not sufficient to explain the observed delays as described, for instance, in Stankov et al. (2017). The remaining effect must therefore be ascribed to the inertia and time scales of the inherent ionospheric recombination and transport processes.

7. Conclusions

In order to obtain a reliable interpretation of the effect of a solar eclipse on the ionosphere, it is important to take into account the full, three-dimensional geometry of the event. Since the ionosphere is significantly extended in the vertical direction, one should not rely solely on the knowledge of the eclipse path at sea-level. We have shown for both the March 2015 and August 2017 eclipses that the differences between the eclipse paths at various altitudes have an observable effect on the location of the maximal TEC depletion.

The geometry, including the variations with height, is highly variable from one eclipse to another. As we have illustrated by showing the results for a series of recent and future eclipses, the degree to which the path of an eclipse varies with altitude depends on the time the eclipse happens and the latitude at which it can be observed. Differences in both the location and timing of the central eclipse tend to be greater at the beginning and end of the event and are usually larger at higher latitudes. However, it is evident from Figures 6–9 that there are significant differences between events and the geometry of each case has to be considered individually.

Finally, it is worth noting that some events are not visible as a total eclipse on the ground but may still cause equally strong effects in the ionosphere. In some cases an eclipse can be observed as total in the visible light only above a certain altitude. Since only altitudes around the peak of the ionospheric electron density are important, such events can be considered total eclipses for the purpose of studying the ionospheric response. It should also be kept in mind that the distinction between total, partial and annular eclipses is not that relevant for ionospheric applications, because in the EUV part of the spectrum all eclipses are partial. Therefore,

eclipses that are total in visible light only at higher altitudes are as important to consider for ionospheric applications as those for which totality extends to sea level.

Acknowledgments

This study is supported by the Belgian Solar-Terrestrial Centre of Excellence (STCE). The `pyephem` Python package is provided freely by B. Rhodes through this website: <https://rhodesmill.org/pyephem/>.

References

- Abidin Abdul Rashid, Z., Awad Momani, M., Sulaiman, S., Alauddin Mohd Ali, M., Yatim, B., Fraser, G., & Sato, N. (2006). GPS ionospheric TEC measurement during the 23rd November 2003 total solar eclipse at Scott Base Antarctica. *Journal of Atmospheric and Solar-Terrestrial Physics*, 68(11), 1219–1236. <https://doi.org/10.1016/j.jastp.2006.03.006>
- Afraimovich, E. L., Palamartchouk, K. S., Perevalova, N. P., Chernukhov, V. V., Lukhnev, A. V., & Zalutsky, V. T. (2000). Ionospheric effects of the solar eclipse of March 9, 1997, as deduced from data from the GPS-radio interferometer at Irkutsk. *Advances in Space Research*, 26(6), 997–1000. [https://doi.org/10.1016/s0273-1177\(00\)00045-4](https://doi.org/10.1016/s0273-1177(00)00045-4)
- Altadill, D., Solé, J. G., & Apostolov, E. M. (2001). Vertical structure of a gravity wave like oscillation in the ionosphere generated by the solar eclipse of August 11, 1999. *Journal of Geophysical Research*, 106(A10), 21,419–21,428. <https://doi.org/10.1029/2001JA900069>
- Bamford, R. A. (2001). The effect of the 1999 total solar eclipse on the ionosphere. *Physics and Chemistry of the Earth, Part C: Solar, Terrestrial & Planetary Science*, 26(5), 373–377. [https://doi.org/10.1016/s1464-1917\(01\)00016-2](https://doi.org/10.1016/s1464-1917(01)00016-2)
- Bretagnon, P., & Francou, G. (1988). Planetary theories in rectangular and spherical variables. VSOP 87 solutions. *Astronomy & Astrophysics*, 202(1–2), 309–315.
- Chauvenet, W. (1863). *A manual of spherical and practical astronomy* (Vol. 1). Philadelphia, PA: J.B. Lippincott & Co.
- Davis, C. J., Clarke, E. M., Bamford, R. A., Lockwood, M., & Bell, S. A. (2001). Long term changes in EUV and X-ray emissions from the solar corona and chromosphere as measured by the response of the Earth's ionosphere during total solar eclipses from 1932 to 1999. *Annales Geophysicae*, 19(3), 263–273. <https://doi.org/10.5194/angeo-19-263-2001>
- Espenak, F. (1987). Fifty year canon of solar eclipses: 1986–2035 (NASA-RP-1178-REV). Greenbelt, MD, USA: NASA Goddard Space Flight Center. available from eclipse.gsfc.nasa.gov.
- Espenak, F. (2014). *Thousand year canon of solar eclipses 1501 to 2500*. Portal, AZ, USA: Astropixels Publishing.
- Espenak, F., & Meeus, J. (2009). Five millennium canon of solar eclipses: –1999 to +3000 (2000 BCE to 3000 CE)—Revised (NASA/TP-2009-214174). Hanover, MD, USA: NASA Center for AeroSpace Information. available from eclipse.gsfc.nasa.gov.
- Hairston, M. R., Mrazek, S., Coley, W., Burrell, A., Holt, B., Perdue, M., et al. (2018). Topside ionospheric electron temperature observations of the 21 August 2017 eclipse by DMSP spacecraft. *Geophysical Research Letters*, 45, 7242–7247. <https://doi.org/10.1029/2018GL077381>
- Hoque, M. M., Wenzel, D., Jakowski, N., Gerzen, T., Berdermann, J., Wilken, V., et al. (2016). Ionospheric response over Europe during the solar eclipse of March 20, 2015. *Journal of Space Weather and Space Climate*, 6, A36. <https://doi.org/10.1051/swsc/2016032>
- Meeus, J. (1985). *Astronomical formulae for calculators* (3rd ed.). Richmond, VA, USA: Willmann-Bell.
- Meeus, J. (1998). *Astronomical algorithms* (2nd ed.). Richmond, VA, USA: Willmann-Bell.
- Mošna, Z., Boška, J., Knížová, P. K., Šindelářová, T., Kouba, D., Chum, J., et al. (2018). Observation of the solar eclipse of 20 March 2015 at the Pruhonic station. *Journal of Atmospheric and Solar-Terrestrial Physics*, 171, 277–284. <https://doi.org/10.1016/j.jastp.2017.07.011>
- Mrazek, S., Semeter, J., Drob, D., & Huba, J. D. (2018). Direct EUV/X-ray modulation of the ionosphere during the August 2017 Total Solar Eclipse. *Geophysical Research Letters*, 45, 3820–3828. <https://doi.org/10.1029/2017GL076771>
- Müller-Wodarg, I. C. F., Aylward, A. D., & Lockwood, M. (1998). Effects of a mid-latitude solar eclipse on the thermosphere and ionosphere - A modelling study. *Geophysical Research Letters*, 25(20), 3787–3790. <https://doi.org/10.1029/1998GL900045>
- Nautical Almanac Office (1961). *Explanatory supplement to the astronomical ephemeris and the American Ephemeris and Nautical Almanac*. London UK: Her Majesty's Stationary Office.
- Rishbeth, H. (1968). Solar eclipses and ionospheric theory. *Space Science Reviews*, 8(4). <http://doi.org/10.1007/bf00175006>
- Rishbeth, H. (1970). Eclipse Effects in the Ionosphere. *Nature*, 226(5251), 1099–1100. <https://doi.org/10.1038/2261099a0>
- Stankov, S. M., Bergeot, N., Berghmans, D., Bolsée, D., Bruyninx, C., Chevalier, J.-M., et al. (2017). Multi-instrument observations of the solar eclipse on 20 March 2015 and its effects on the ionosphere over Belgium and Europe. *Journal of Space Weather and Space Climate*, 7, A19. <https://doi.org/10.1051/swsc/2017017>
- Vallado, D. A. (1997). *Fundamentals of astrodynamics and applications*. New York, USA: The McGraw-Hill Companies, Inc.
- Verhulst, T. G. W., Sapundžiev, D., & Stankov, S. M. (2016). High-resolution ionospheric observations and modeling over Belgium during the solar eclipse of 20 March 2015 including first results of ionospheric tilt and plasma drift measurements. *Advances in Space Research*, 57(11), 2407–2419. <https://doi.org/10.1016/j.asr.2016.03.009>
- Verhulst, T. G. W., & Stankov, S. M. (2017). Height-dependent sunrise and sunset: Effects and implications of the varying times of occurrence for local ionospheric processes and modelling. *Advances in Space Research*, 60(8), 1797–1806. <https://doi.org/10.1016/j.asr.2017.05.042>
- Verhulst, T. G. W., & Stankov, S. M. (2018). Ionospheric wave signature of the American solar eclipse on 21 August 2017 in Europe. *Advances in Space Research*, 61(9), 2245–2251. <https://doi.org/10.1016/j.asr.2018.02.007>
- Weisstein, E. W. (2020). “Circle-Circle Intersection” from MathWorld—A Wolfram web Resource. <https://mathworld.wolfram.com/Circle-CircleIntersection.html>